THE PENNSYLVANIA STATE UNIVERSITY
SCHREYER HONORS COLLEGE

DEPARTMENT OF CHEMICAL ENGINEERING

INCORPORATING NANOSCALE COMPOSITES INTO STEREOLITHOGRAPHIC PRINTING TECHNIQUES FOR THE OPTIMIZATION OF MEMBRANE ELECTROCHEMICAL PROPERTIES

CHRISTOPHER MALENCIA
SPRING 2016

A thesis
submitted in partial fulfillment
of the requirements
for a baccalaureate degree
in Chemical Engineering
with honors in Chemical Engineering

Reviewed and approved* by the following:

Michael Hickner
Associate Professor of Materials Science and Engineering, Chemical Engineering
Thesis Supervisor

Darrell Velegol
Distinguished Professor of Chemical Engineering
Honors Adviser

* Signatures are on file in the Schreyer Honors College.

ABSTRACT

Fuel cells and portable electrochemical devices serve as environmentally friendly alternatives to fossil fuel technologies for the portable electronic and transportation sectors. Proton exchange membrane fuel cells (PEMFCs), batteries, and other fuel cells utilize ion exchange membranes or polymer electrolyte membranes between cathodic and anodic reactions. The incorporation of nanoparticles and nanoscale composites leads to optimal conductivities and stabilities of these electrochemical membranes. Composite polymer synthesis conventionally follows a solution casting method. Stereolithography, or 3D-printing through photopolymerization, offers an advantageous alternative and can produce high surface area membranes. This thesis proposes the utilization of 3D-printing techniques in synthesizing composite polymer membranes for electrochemical applications.

Six major 3D printing techniques include stereolithography, digital light processing, fused deposition modeling, selective laser sintering, electronic bean melting, and laminated object manufacturing. Polymer membranes require high precision in both printer resolution and chemical composition. Stereolithographic and digital light processing techniques offer ideal pathways for creating specialized membranes. Both printing techniques were utilized to introduce composite doping into the Penn State 3D printing laboratory. Hydrophobic and hydrophilic clays were compared at varying additive concentrations; resin properties and mechanical testing highlighted hydrophilic clays as an ideal additive to the poly(ethylene glycol) dimethacrylate and polyurethane resins used. Non-uniform compositions across hydrophobic prints suggested that hydrophobic composite doping was ill suited for printing the resins-clay mixtures.

TABLE OF CONTENTS

LIST OF FIGURES

LIST OF TABLES

ACKNOWLEDGEMENTS

The completion of this thesis report would not have been possible without the support offered both within and without the laboratory. I would like to thank Dr. Mike Hickner for his direction in developing this project, support in gaining access to analysis equipment, and advice when compiling the final report.

To Sean Nuñez, thank you for your unfailing support in troubleshooting the printing equipment. Thanks to Robert Kaminsky, and Jiho Seo for training and guiding me through both the resin synthesis and photopolymerization processes. I would like to thank Dr. David Shelleman for training on the mechanical break test equipment.

To all family and close friends who have followed this project to its completion, your support morally, intellectually, and otherwise, could not be undervalued.

Chapter 1 Introduction to Polymer Electrolytes and Membranes

Polymer electrolytes (PEs) and proton exchange membranes (PEMs) have been an increasingly popular subject of study due to their flexibility, stability and room temperature conductivity. In recent efforts to improve the conductivity of such materials, researchers have considered the addition of nanoparticles and nanoscale ceramic fillers. The implementation of such particles into a polymer lattice increases the conductivity without compromising stability. The increase in conductivity leads to the implementation of these new composite polymers in portable electrochemical devices such as fuel cells, solar cells, and advanced batteries. Varying synthesis methods of composite polymer membranes lead to different structural and electrochemical changes following the introduction of nanoparticles into the polymer electrolyte matrix. Analysis of membranes with nanoparticle doping has extended from commercially available PEM products such as Nafion, to PE applications including high temperature polybenzimidazole membranes.

The search for renewable and clean energy sources attempts to satisfy society's ever growing need for power. As reserves of natural energies deplete, the demand for alternative energy will support development of unconventional energy technologies. Nuclear, solar, water and wind energy sources may provide these alternatives for power grids and large-scale power production. The transportation sector, on the other hand, has struggled to cut back its dependence on fossil fuels. Recently, electric vehicles became an obvious opportunity to step away from greenhouse gas producing gasoline and diesel engines; battery technology is currently stepping into the automotive market, but faces significant hindrances in becoming a long-term substitute for fossil fuel technologies.[1]

The Fuel Cell

Fuel cell technology offers a small-scale electric energy conversion device perfect for automotive energy needs. A fuel cell works similarly to a battery, where a chemical reaction produces electricity. While batteries use a contained electrolyte in a closed system, fuel cells utilize flowing reactant and product streams. Battery technologies favor energy dense chemicals that can sustain a high potential difference between electrodes, but these chemicals are often environmentally harmful once the battery expires[1]. Fuel cell reaction streams do not generate high voltages for the production of electricity, but are much more environmentally friendly; consider the reactants and products in **Figure 1**.

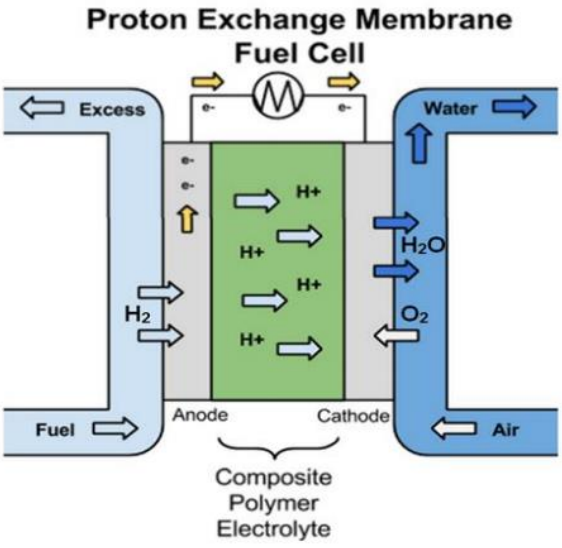

Figure 1: Composite polymer electrolytes utilized in proton exchange membrane fuel cells.

Fuel cells aligned in series increase voltage for use with high-power electric motors, such as in automobiles.[2] The interface itself differs between fuel cell design types, and ion transfer is necessary for the continuous buildup of charge across electrodes. Various designs use alkaline solutions, molten salt solutions, solid oxides and other liquid or solid electrolytes. One of the most popular types of fuel cells for low temperature use, proton exchange membrane fuel cells (PEMFCs) utilize ion conducting membranes or polymer electrolytes to facilitate charge transfer.

PEMFCs

In PEMFCs, ion conduction between cathode and anode interfaces occurs between polymer electrolytes or ion conducting polymer exchange membranes. PEs are formed by dissolving salts into a polymer lattice; without the addition of these ions, most polymer solutions lack charged particles that promote charge transfer.[3] The salt additive acts to disrupt the crystallization of the polymer and create large amorphous regions in the polymer structure. Amorphous regions function as ion channels for improved ion diffusion through the polymer.[3] Ion conducting polymer membranes have ion channels but are synthesized without the electrolytic salts required in PE synthesis. Such membranes, including Nafion and similar sulfonated polymers, are high modulus materials that serve as effective separators between the anode and cathode streams in fuel cells.[4]

Polymer electrolytes and proton exchange membranes have shown clear advantages over their liquid electrolyte counterparts. Research into using polymer membranes aims to optimize key PE and PEM characteristics including thermal stability, corrosion, reactant crossover, wettability and conductivity. While conductivity of polymers increases with temperature, thermal stability of polymer chains and structures must be considered at elevated temperatures.[5,6] Moreover, ideal membrane and electrolyte systems operate at room temperature where heat transfer elements are of much less concern.

While PEMs function well at moderate temperatures, polymer electrolytes at room temperature normally demonstrate low conductivity and tend to crystallize.[6,7] Attempts to improve the room temperature conductivity of PEs involve the substitution of larger salt anions, alternative polymer structures, and different sidechains.[7] One of the most promising improvements to polymer electrolytes is the addition of nanoscale ceramic fillers including SiO_2, Al_2O_3, TiO_2 and CeO_2.[2,9] The nanoparticle fillers interact with both the polymer and the salt ions to form a new complex.[3,8] Lewis acid-base interactions between the nanoparticles and the polymer network enhance the density of amorphous zones throughout the membrane structure. The advantages of nanocomposite doping extends to ion exchange membranes as

well. The nanoparticles can interact with the anions and cations of PEs or the existent channel structures within PEMs to form additional pathways through which charged particles move.[4,10,11]

Chapter 2 Composites in Conventional Membranes

Techniques for incorporating nanoparticles into polymer electrolytes and ion exchange membranes are similar to normal membrane synthesis. Effects of nanoparticles on polymer membranes can be studied empirically through two main characterization techniques. The electrochemical interactions between the filler particles and the polymer material are evident in the changes in membrane conductivity.[1,5,10,12,13] Structural disruptions caused by filler particles within the polymer complex can be monitored with differing nanoparticle concentrations.[5,9]

Synthesis Techniques

There are several methods for creating the nano-scale particles and fillers to be introduced into the polymer/salt complex or ion exchange polymer lattice. Many of the pathways involved in nanoparticle creation involve a production reaction followed by several stages of drying and heating to remove solvents and impurities.[9,14,15] An example of this would be the production of cesium oxide, a common polymer composite additive. In cesium oxide production, an aqueous ceric ammonium nitrate solution is combined with an aqueous solution of citric acid. The mixture is heated until an evaporation leads to the formation of a polymer gel. This gel is burned and the resulting cesium oxide powder is calcined to remove any remaining impurities.[9] The main technique for synthesizing composite polymer electrolytes is called solvent casting.[5,11,14] Various solution casting methods utilize similar steps. A mixture of the pure polymer and electrolytic salt is stirred until well mixed. The nanoparticles are introduced, the mixture

blended, and the solution set into a mold. Membranes can also be molded with nanoparticles before the introduction of electrolytes. Depending on the composite membrane diffusion properties, soaking casted membranes in an electrolyte brine can be sufficient for CPE synthesis.[3,16] For ion exchange membrane doping, composite membrane synthesis is more straightforward. Soaking membranes in a solution of dispersed nanocomposites will lead to the integration of composite particles into the membrane structure.[4]

Structural Changes

Polymer electrolytes undergo changes in their structure both with addition of electrolytic salts and with the addition of ceramic fillers or nanocomposites. The densities of amorphous and crystalline regions within PEs significantly affect the polymer's chemical and physical properties.[3,5,9] The addition of a salt to the original polymer solution disrupts the crystalline nature of the polymers, and adding the ceramic fillers further reduces the risk of recrystallization.[6,7] Atomic force microscopy (AFM), x-ray diffraction (XRD), and scanning electron microscopy (SEM) are commonly utilized for the study of physical changes in polymer structure.[3,4,5,9,14,17] In Figure 2, AFM was used to capture images of a composite polymer electrolyte (CPE), in this case poly(ethylene oxide) (PEO). AFM took pictures of the PEO complexed with KI and KI with the ceramic filler CeO_2.[9]

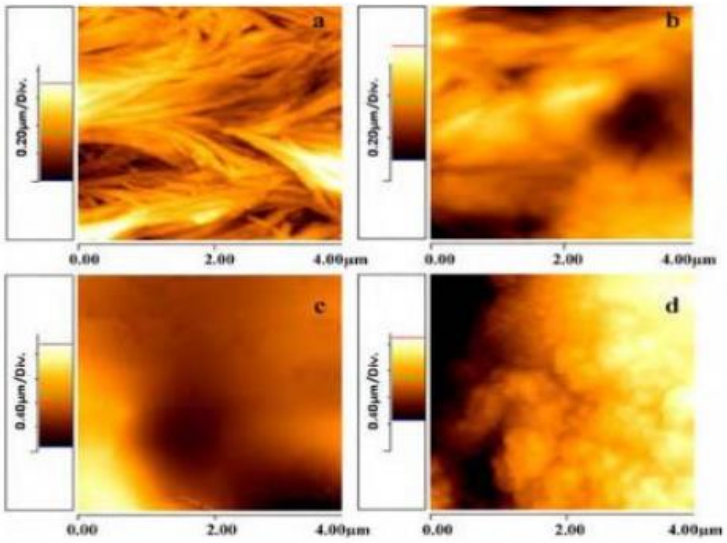

Figure 2: Topographic atomic force microscopy.[9]

Image A displays pure PEO with spherulites branching out through the polymer, and the formation of these spherulites is associated with polymeric crystallinity. The AFM image reflects the semi-crystalline nature of pure PEO. Image B shows the polymer electrolyte of PEO mixed with KI salt. Evidently, the polymer electrolyte undergoes a breakdown of the spherulite structure and the crystalline network of pure PEO. A complete breakdown of spherulite structures comes with the addition of CeO_2 . In image C, no crystallization is present and the polymer is nearly flat. This image corresponds to the composite polymer electrolyte with 20% wt. CeO_2. The last image, D, has 25% wt. CeO_2 and it demonstrates a new type of crystallinity forming in the polymer. Determining the ideal morphology, C or D, becomes clear with conductivity analyses of the different composition CPEs. The AFM images all conclude that the addition of ceramic fillers reduces the ability of the polymer electrolyte to crystallize; larger amorphous regions through which charged particles travel develop as crystallinity breaks down, increasing conductivity.[9]

In Figure 3 XRD analysis is used to characterize poly(vinylidene fluoride-hexafluoro propylene), PVdF-HFP, with and without the addition of a nanocomposite. The introduced filler composite becomes a solid plasticizer that increases membrane transfer properties.[10,11,13]

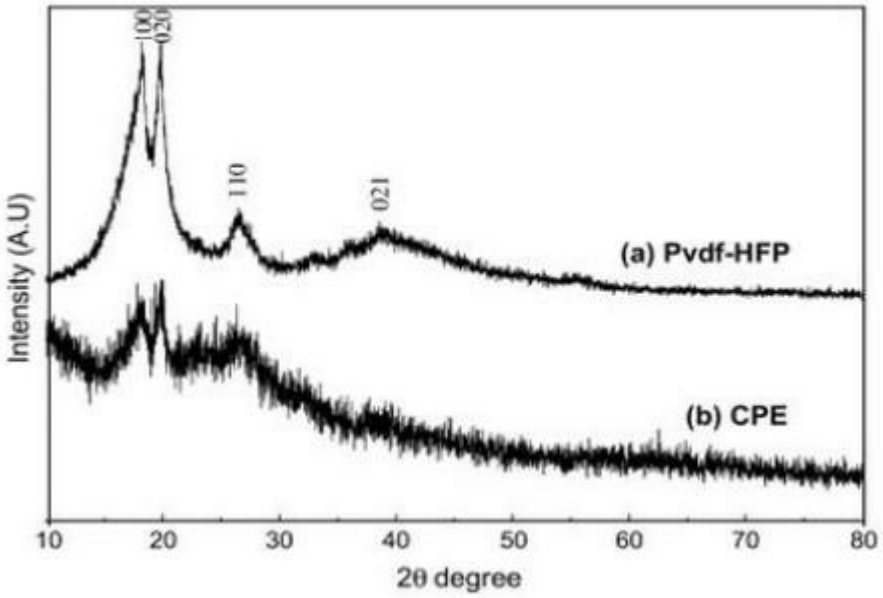

Figure 3: XRD patterns of: (a) polymer and (b) composite polymer electrolyte.[13]

The XRD spectra compares doped to pure PVdFHFP polymers by analyzing four main peaks. These peaks, labelled by Miller indices (100), (020), (110) and (021), correspond to different crystallinities of PVdF-HFP. The semi-crystalline polymer structure defined by these peaks is evidently stronger in the pure, undoped polymer. With the addition of the inert filler particles, XRD peaks both decrease in intensity and broaden.[13] Consistent with other analysis techniques and similar nanocomposite doping experiments, chain reorganization and high filler ionic conductivities are responsible for restructuring of the crystalline polymer structures.[5,12]

Proton exchange membranes, with existing ion channel structures, do not change as significantly with the addition of nanocomposites.[4] The integration of nanoparticles into the PEM structure occurs readily as the membrane is immersed within a solution of dissolved nanoparticles. The extent to which nanoparticles penetrate into the ion membrane structure depends on the liquid solvent and particle

compositions. Nafion membranes have been analyzed after Fe_2TiO_5 particle doping under water and ethanol solvents.[4] For both ethanol and water solvent trials, high concentrations of nanocomposite particles lead to particle aggregation and decreased uptake. The solvent composition, water or ethanol, dictated deposition of nanoparticles in hydrophilic or hydrophobic regions in the PEM respectively.[4]

Electrochemical Changes

Polymer electrolytes and proton exchange membranes vary in electrochemical properties based on polymer composition, synthesis methods, and additive concentrations.[1,4,8,10,14] Incorporation of nanoparticles into the polymer matrix adds another variable for optimizing properties such as conductivity and exchange capacities. Moreover, while physical changes in polymer matrices are more easily predictable, electric properties are rarely monotonic with changes in component concentrations.[3,4,5,6,14,15] Proton conductivities and ion exchange capacities for PEs can be modeled through activation energy calculations or measured through ion uptake titrations and analysis techniques like electrochemical impedance spectroscopy (EIS) and frequency response analysis.[2,5,6,11,17] Modeling conductivities through polymer activation energies considers the intermolecular forces between composites and the polymer electrolyte. Lewis acid-base interactions between the nanoparticle filler molecules and the polymer/salt complex disrupt the symmetry within the polymer structure, allowing more salt ions to pass freely through the polymer. The increase in polymer conductivity has been attributed to this disrupted structure phenomenon, and the conductivity of polymer electrolytes, both pure solutions and with nanocomposite doping, can be modeled using the Vogel-Tammann-Fulcher equation:

$$\sigma(T) = AT^{-1/2}\left\{-B\left[R\left(T - T_0\right)\right]\right\}$$

R is the universal gas constant, B is the activation energy, A is a pre-exponential factor, T_0 is the reference temperature and T is the absolute temperature.[6,15]

Continuing with the example of PEO complexed with KI and KI with the ceramic filler CeO2 in the AFM study above, changes in PEO electrochemical properties with varying filler concentrations were given. Conductivities garnered from the Vogel-Tammann-Fulcher equation were compiled in Table 1 with the apparent activation energies of composite polymer electrolytes with different compositions.[9]

Table 1: Room temperature ionic conductivity and activation energy of composite polymer electrolytes.[9]

Sample	σ (S-cm^{-1})	E_a (eV)
PEO_{15}-KI	1.53×10^{-5}	0.38
PEO_{15}-KI-CeO_2 3 wt.%	2.71×10^{-4}	0.21
PEO_{15}-KI-CeO_2 5 wt.%	7.19×10^{-4}	0.16
PEO_{15}-KI-CeO_2 8 wt.%	4.55×10^{-4}	0.17
PEO_{15}-KI-CeO_2 10 wt.%	3.17×10^{-4}	0.13
PEO_{15}-KI-CeO_2 15 wt.%	1.16×10^{-3}	0.12
PEO_{15}-KI-CeO_2 20 wt.%	2.15×10^{-3}	0.07
PEO_{15}-KI-CeO_2 25 wt.%	6.89×10^{-4}	0.11

The data given clearly show improvements in the room temperature conductivity of polymer electrolytes with the addition of nanoparticles. However, the activation energy increases as the concentration of CeO2 moved from 20% to 25%, and the conductivity decreases. These changes can be attributed to the differences in the polymers crystallization shown in the previous AFM images. High amount of ceramic filler have been predicted to clog up the ion channels and decrease diffusion rates. Since the exact mechanism for nanoparticles and polymer electrolyte structure interactions is unknown, the phenomenon causing the decrease in conductivity with increased concentration is uncertain.[9,15]

Considering room temperature conductivity of polymer electrolytes can be improved with the addition of nano-particles, the enhancement is not limited to room temperature experiments. The composite polymer electrolyte conductivity stays several fold higher than that of the pure PE solution through a wide temperature range.[5] Nonetheless, the conductivity gap between doped and pure polymers is much greater at lower temperatures.[15]

In Figure 4, strontium cerate nanoparticles, SrCeO3, were studied for their effects on polybenzimodazole (PBI) with applications PEMFC membranes. For increased chemical and thermal resistance, PBI membranes were first doped with phosphoric acid (PA) before the addition of nanoparticles.[5]

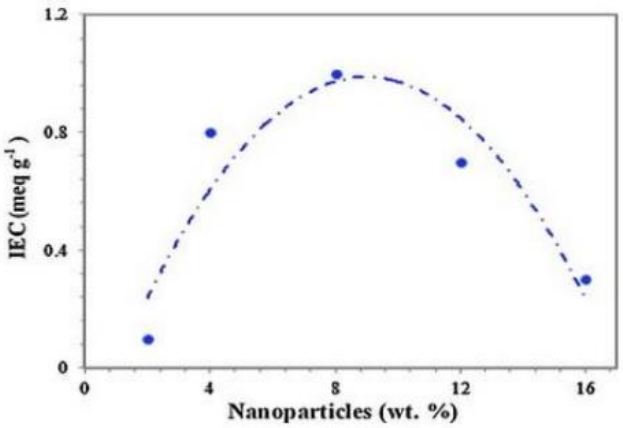

Figure 4: Maximum ion exchange capacity at nanocomposite doping percent.[5]

Ion exchange capacities for phosphoric acid doped composite PBI membranes were studied via a simple sodium hydroxide titration following extended immersion in a sodium chloride bath. Phosphoric acid doping, by itself, increases dissociable H+ ion concentrations, boosting IECs of the membrane. Optimum ion exchange capacity based on nanoparticle concentration resulted at 8 wt% nanoparticles where maximum acid uptake could occur. The optimized 8 wt% PA-PBI membranes were integrated into platinum loaded PEMFC for thermal stability measurements.[5]

Integration of composite nanoparticles into polymer electrolytes causes structural deformations in the polymer matrix and changes in electrochemical properties. While composite polymer electrolytes often show higher conductivity than pure polymer electrolytes, physical and electrical properties with varying nanoparticle doping concentrations are rarely monotonic. Understanding the mechanisms behind the incorporation of nanoscale fillers into the polymer will be paramount to optimizing composite polymer electrolytes.

Ion conductivities for composite proton exchange membranes depends on the location of composites within the PEM structure. As previously mentioned, water and ethanol solvents have been utilized to investigate particle deposition in respective hydrophilic and hydrophobic regimes.[4] In Figure 5, proton conductivity measurements are plotted for Nafion membranes at varying solvent compositions and nanoparticle doping concentrations.[4]

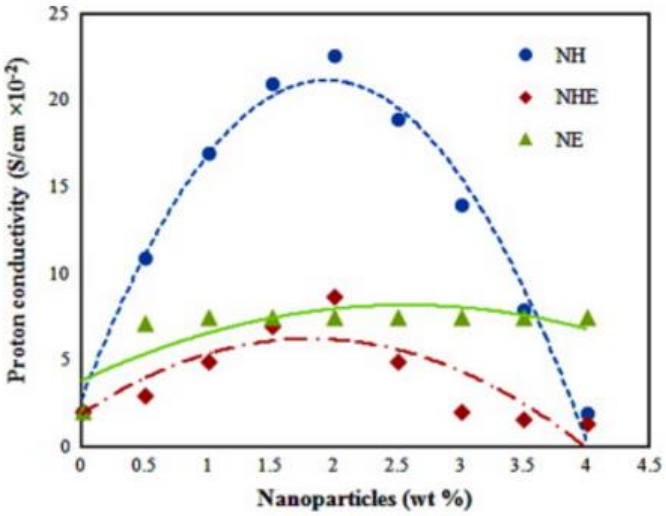

Figure 5: Composite doping in a Nafion proton exchange membranes.[4]

Solvents utilized for the proton conductivity study were pure water (NH), 1:1 water and ethanol (NHE), and pure ethanol (NE). Proton conductivity within PEMs relies on interactions between hydrolyzed atom sites (SO_3^- and H_3O^+) which occur between sulfonated membrane molecules and water molecules. NH trials included the deposition of nanoparticles in hydrophilic sections of the membrane, causing microscopic swelling. The swelling more readily permitted interactions between water and sulfonated molecules to facilitate proton conductivity. For samples with ethanol solvents, NE and NHE, microscopic swelling occurred at hydrophobic regions where SO_3^- and H_3O^+ interaction did not occur. The positive influence of nanoparticle doping on conductivity was not evident when ethanol solvents were used for nanoparticle deposition. Optimum proton conductivity within PEMs requires specific synthesis methods.[4]

Chapter 3 Introduction to 3D Printing Techniques

Material printing technologies are an emerging science, first gaining ground with the invention of the inkjet printer in 1976. The successful printing of three-dimensional objects from digital data, known as stereolithography, was developed in 1984 for modeling manufacturing products before full production. The various printing techniques developed since can be categorized following six general groups: stereolithography, digital light processing, fused deposition modeling, selective laser sintering, electronic bean melting, and laminated object manufacturing.[18-29]

Stereolithography

While stereolithography (STL) is the oldest of the free form printing techniques, it is still utilized in several manufacturing and research fields today. Stereolithographic techniques require a liquid polymer that can be solidified through ultraviolet exposure. Printed objects are created in computer modeling software, such as computer aided design (CAD) programs. Designs are 'sliced' into thin layers that are printed consecutively.[18] The STL method is displayed in Figure 6:

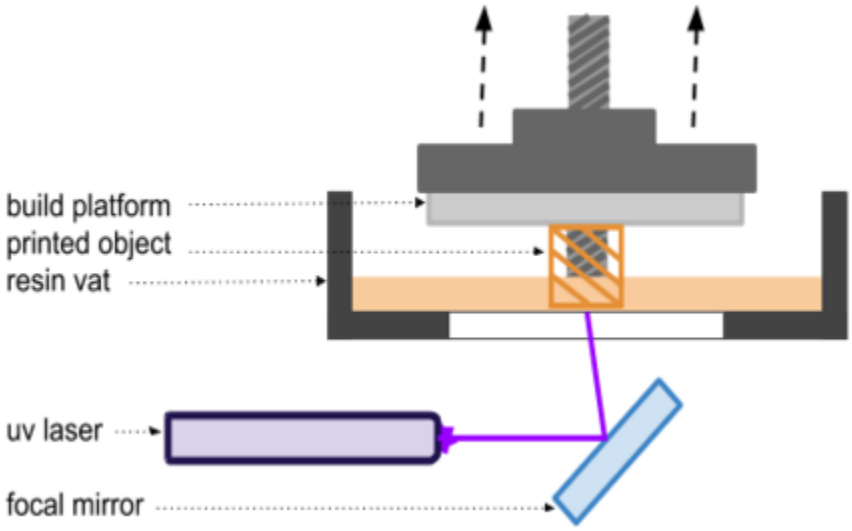

Figure 6 Stereolithographic techniques utilize a UV laser to polymerize resin

Polymerizing resin is contained in a vat and incident light either shines onto the top of the resin or through the vat's clear base. The resin undergoes photopolymerization and solidifies onto a building plate. Layer by layer, ultraviolent light cures an object specified by the CAD file. The receding build plate pulls the solid object from the resin where it is fully cured in an ultraviolet oven.[18] Since STL uses a concentrated laser, high resolution, on the order of 20µm, is achievable.[19] Most free form printing technologies can only reach an accuracy of 50-200µm. With the capability of micron and sub-micro scale resolution, stereolithography offers an ideal technology for biomedical engineering and other high precision purposes.

Digital Light Processing

Similar to stereolithographic techniques, digital light processing (DLP) involves the projection of photons to photopolymerize a polymer resin. Instead of using a concentrated ultraviolet laser, DLP displays high intensity light from more typical light sources; similar display technology is used in movie

projectors and cell phone screens.[20] An optical lens is utilized to focus the beam into a high intensity, photon rich display that polymerizes the resin with high precision, see Figure 7.

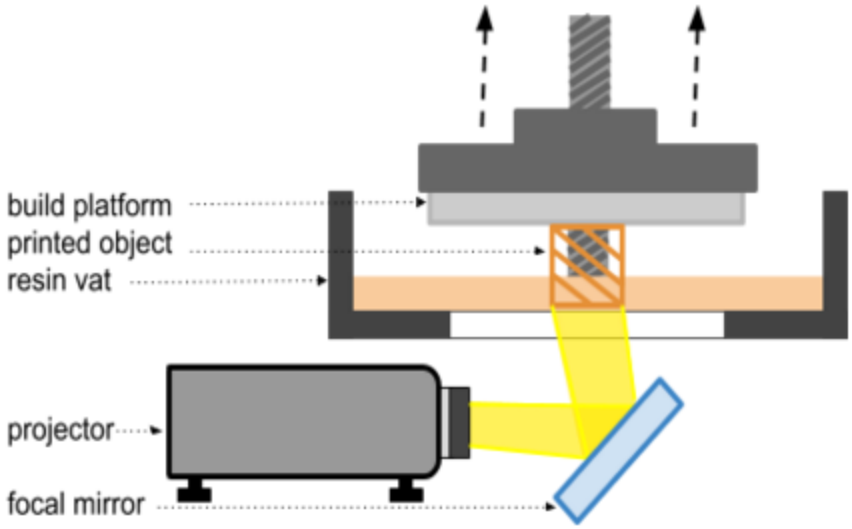

Figure 7: Digital light processing methods project a high volume of protons to polymerize a printed layer.

DLP printing offers fast assembly with short curing times for the solidification of each consecutive layer.[20,21] Compared to SLA setups, DLP printers are much simpler to design for amateur 3D printing groups and can use readily available commercial projectors while maintaining high print resolution.

Fused Deposition Modeling

Printing techniques outside of stereolithography and digital light processing methods do not use photopolymerization mechanisms to create printed objects. Fused deposition modeling (FDM) involves the extrusion of a plastic to draw the 3D object layer by layer. A depiction of the FDM process, also known as fused filament fabrication (FFF), in Figure 8 displays the significant differences between FDM and STL techniques discussed earlier.

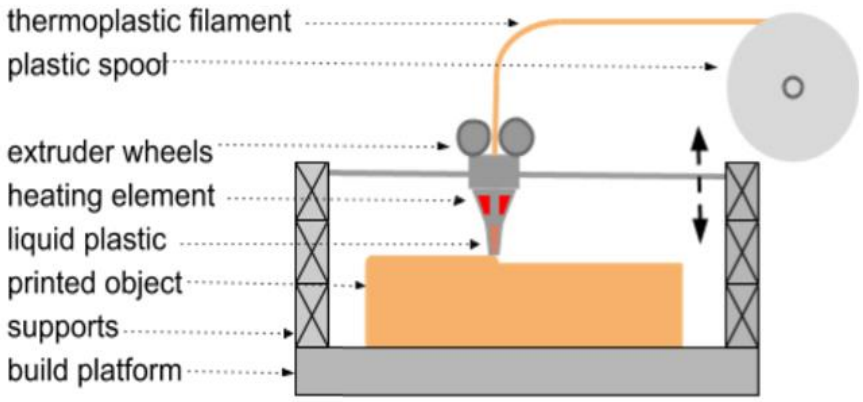

Figure 8: Fused deposition modeling prints by melting a thermoplastic filament in successive layers.

Commercially available filaments that can be purchased in spools are fed to the FDM system. Extruder drive wheels pull the flexible thermoplastic filament into the printer nozzle; a heating element within the nozzle melts the plastic. The thermoplastic cools and solidifies after being deposited on the printed object surface, and heat from depositing plastic fuses successive layers together. The printer's nozzle assembly moves in a horizontal x-y plan to draw each layer according to a digital model. Motors at the printer supports move the system vertically for depositing additional layers. Some FDM systems include a second nozzle for printing supports or creating objects with several thermoplastic components.[22]

Fused deposition modeling printers are inexpensive, as they printers lack complex optical devices required by other printer types; other 3D printers have even manufactured FDM parts. FDM models face challenges including long printing times and low resolution. Unlike optical printing techniques, deposition modeling cannot quickly fill a large solid area within a layer. Printing times are increased as the extruded must manually fill in the print areas similar to using an ink pen to color in a solid shape.

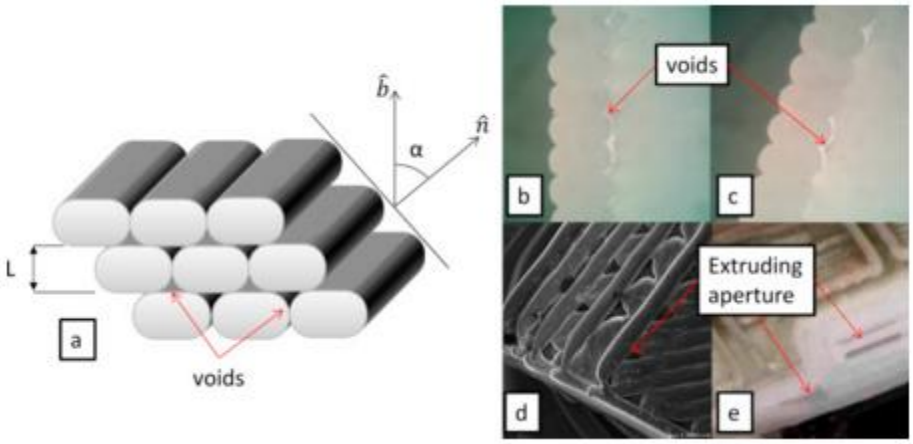

Figure 9: FDM printers face challenges with non-uniform composition (a, b, c) based on aperture (d, e).[22]

Resolution of FDM prints is dependent on nozzle size, and such methods cannot reach resolutions on the same scale as STL and DLP techniques (Figure 9).[22] Moreover, consistency in the macrostructure of FDM prints is difficult to ensure, a voids are present in the structure. The fused deposition modeling and fused filament fabrication technique is utilized for rapid prototyping, custom models, and prosthetics applications.

Selective Laser Sintering

Selective laser sintering (SLS) combines aspects of both STL and FDM by using high-powered lasers to heat print materials. Unlike the ultraviolet and visible light beams employed by stereolithography and digital light processing respectively, SLS utilizes infrared lasers for printing each layer, as depicted in Figure 10. Sintering involves the formation of a solid mass through applied heat or pressure without fully melting the original powder material.[23,24] A similar process to SLS, known as selective laser melting, completely liquefies metal powders to form each print layer.

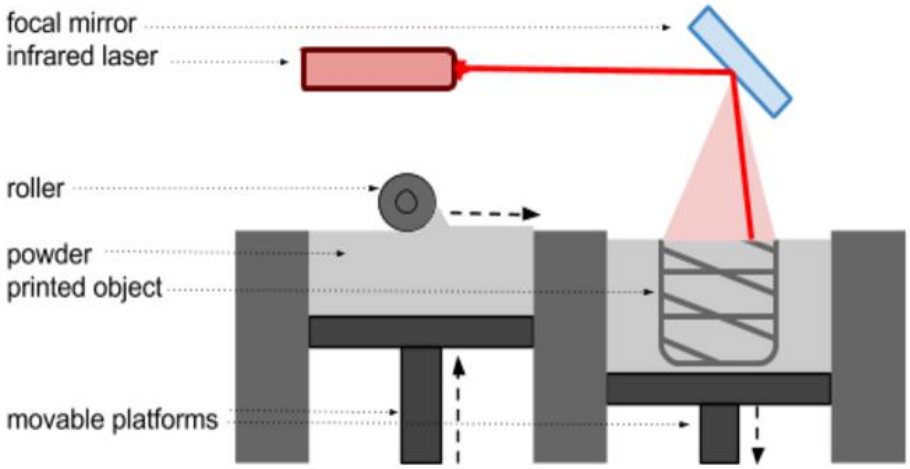

Figure 10: SLS techniques sinter and print material from a powder bed using an infrared laser.

A powerful infrared incident beam, commonly supplied from a carbon dioxide laser, partially melts powdered particles or binder materials in the desired layer shape. The sintering platform then lowers, and a roller supplies another layer of powder for sintering. Refilling powder is supplied by another powder bed and movable platform. Print layers, typically around 100 µm, are added sequentially until the entire object is solidified within the powder bed.[23] By printing the object within a powder bed, SLS printing avoids the need for object supports that are required by STL and FDM techniques.[25] Selective laser sintering is renowned for being able to produce models with complex geometries quickly and at low cost.

The SLS procedure faces challenges unique to this method of printing, and sintering powder composition is a significant variable for producing successful prints. Across most powder and binder choices, uniform density is difficult to achieve due to temperature, gravity, and capillary effects.[25] Failures of SLS printed objects include surface pores, cracking, and loose powder inclusion, all of which decrease the durability of printed components. Sintering conditions are varied based on powder composition and desired print resolution, and selective laser sintering has been used across manufacturing and modeling disciplines from healthcare implant fabrication to aerospace product design.[23-25]

Electron Beam Melting

Similar to selective laser melting techniques, a subset of SLS, electron beam melting (EBM) creates printed layers from melting a powder. Electromagnetic forces are used to generate and manage an electron beam from free electrons in a vacuum, see Figure 11. Incident electrons transfer kinetic energy on a powder bed where heat melts successive layers of a printed object.[26]

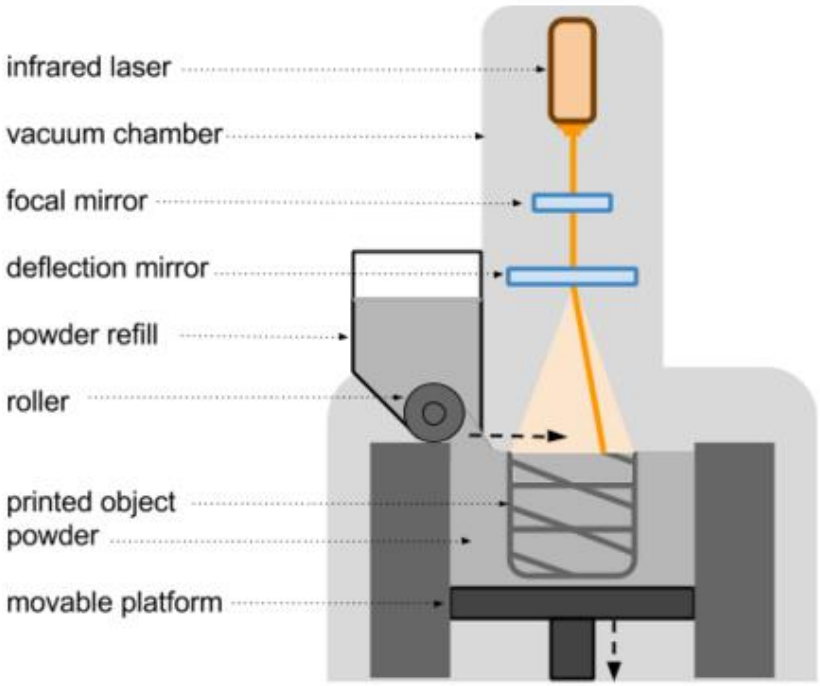

Figure 11: EBM techniques fully melt print material layers with an electron beam within a vacuum.

Electron beams melting can be more advantageous than other 3D printing techniques based on desired applications. Due to the high energy density of an electron beam, powder melting can occur more readily with EBM than with laser-based methods.[27] Faster printing times can be achieved, particularly when beam splitting can melt and solidify many parts of the print layer at once. As with SLS, EBM can produce complex structures within the powder bed avoiding the need for support structures.[27,28]

While electromagnetic radiation can propagate through gas, the electron beam requires a high vacuum environment. Due to the complexity of the electron beam design and high vacuum requirements, EBM techniques are utilized exclusively for metallic substances such as Titanium and Chrome-Cobalt alloys.[26,28] The high vacuum environment and introduction of inert helium gas during metallic powder melting permits a high specificity in printed metal material properties; thermal curing and chemical milling of metal parts is not required in EBM as compared to other metal part manufacturing technologies.[28] Industrial applications include medical implants, aerospace turbines, and automotive turbos.[26-28]

Laminated Object Manufacturing

The laminated object manufacturing (LOM) technique is the only method of the six popular 3D printing processes that does not require solidifying or melting a liquid or powder. Instead, LOM creates prints by successively layering sheets of material with adhesive backings, see Figure 12. Lamination can be tailored for a variety of printer material sheets including paper, plastics, and metals.

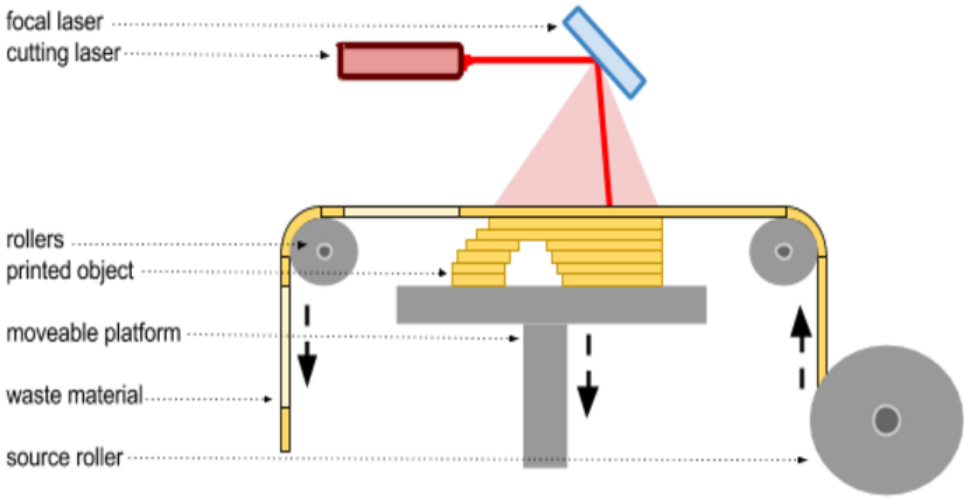

Figure 12: LOM techniques layer material sheets with adhesive backing by cutting layer shapes.

Freshly rolled print material is layered onto the print platform where heated rollers cure the adhesive. Either an incident laser or physical cutting apparatus cuts the shape of a layer and crosshatches unwanted sections for easy removal. The rollers rise and a fresh sheet of material is brought above the object; the cycle continues until the print is finished.

Most printing techniques need to solidify the entire are of a print layer. By starting with a solid sheet, LOM only needs to apply incident laser light to the circumference of a layer shape; fast LOM printing rates are readily achievable.[29] Print layer thickness depends on material sheet thickness, and high resolution prints through laminated object manufacturing are not viable. Due to the physical constraints of cut-away printing, certain geometries are difficult to produce, specifically hollow pieces. Furthermore, low quality surface finishes often require refinishing process after LOM.[29] Laminated object manufacturing is best for prototyping and small order manufacturing as material waste can be high. The main consumer base focusses on architects, artists, and product developers who aim to create inexpensive models.[29]

Composite Doping with Photopolymerization

Membrane synthesis requires high precision and uniform chemical composition of printed polymer material. Selective laser sintering and electron beam melting are better suited for ceramic and metal powders while laminated object manufacturing lacks the precision for membrane manufacturing.[23-25,29] Both stereolithographic and digital light processing techniques are well suited for high resolution, accurate polymerization.[18-21] Three-dimensional printing of membranes has been conducted on photopolymerizable resins, as seen in Figure 13, and compared to membrane casting techniques.[30]

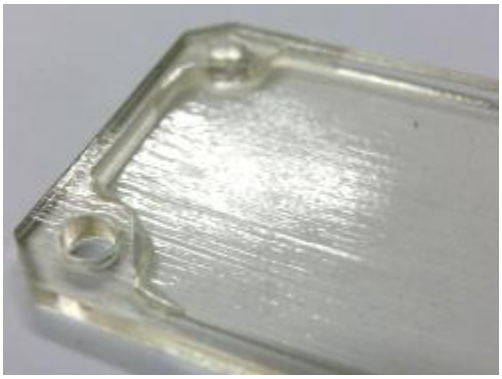

Figure 13: Three-dimensional printing of polymer membranes yields material grains.[30]

In the image of the Tangoplus 3D printed polymer above, material grain appears through the printed membranes, and grain characteristics are based both on print orientation and resolution. Polymer membrane printing has also been conducted at the Penn State laboratory with resins similar to those utilized in this experiment, without composite doping. Mechanical testing of membranes focusses on tensile bar tests under atmospheric, high humidity, and elevated temperature conditions where Young's modulus, tensile strength, or percent elongation data are reported.[31-33] The addition of nanocomposite clay has increased Young's modulus values and decreased percent elongation in tensile testing of some polymer membranes and films.[31,32] Nanocomposite addition can also directly inhibit the polymerization mechanism required for stereolithography and digital light processing.[34,35]

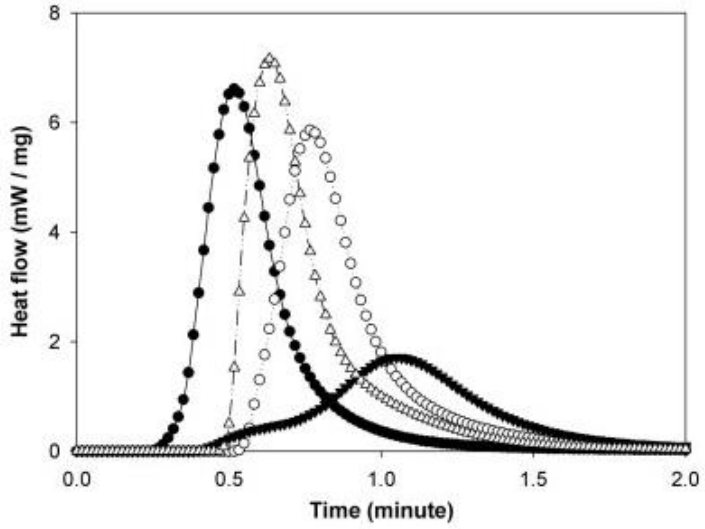

Figure 14: Neat polymer curves (left) show faster photopolymerization kinetics than doped resin curves (right).[34]

In Figure 14, polymerization kinetics were studied by analyzing heat flow with a differential scanning calorimeter.[34] Resin used was a combination polyethyleneglycol diacrylate (PEGDA)and tripropyleneglycol diacrylate (TrPGDA) of with organoclay additives. The curing of neat PEGDA/TrPGDA resin was characterized by solid circles (●) and has the fastest photopolymerization kinetics. Empty triangles (Δ) depict non-reactive clay additives, empty circles (○) depict acrylated polymerizable organoclays, and solid triangles (▼) depict thiolated polymerizable organoclays.[34] All clay additives decrease polymerization kinetics, but the extent of inhibition depends on particular additives.

The influence of clay nanoparticle additives on photopolymerization reactions utilized by STL and DLP printing techniques depends on both clay and resin composition.[31-35] This experiment aims to investigate the influence of hydrophilic and hydrophobic clays on polymerizable resin.

Chapter 4 Experimental

Equipment

At Penn State, and under the direction of Dr. Mike Hickner, a three-dimensional printing lab includes studies on both photopolymerization and extrusion techniques. While exclusively commercial filaments are used for filament deposition modeling, both commercial and synthetized resins are applied to stereolithography and digital light processing printers. The lab is based in room 111 Research Unit A—Modular Lab, and for more specific location details, see Appendix B. Three main pieces of equipment for photopolyerization experiments include a simple projector design, a programmable DLP printer, and a commercial STL printer.

The projector setup is uses an EPSON EX5210 LCD projector, focal lens, flat mirror, and resin dish, see Figure 15. Projected images are displayed by loading a PowerPoint document with slides of each desired layer as a white shape on a black background.

Figure 15: An EPSON proctor, mirror, and lense creates a remedial DLP system.

Resins can be contained and polymerized within a petri dish, and exposure times for each printed layer are dictated manually. While this DLP system is uncomplicated, it is also severely limited. Layer height is imprecise and tall object printing is extremely difficult. Printing times are long and require

constant manual input. The setup is used primarily to test synthesized resins for their respective abilities to polymerize. Photo initiator powders are added to synthesized resin recipes, and simple DLP experiments can be used to gauge correct levels of initiator ratios. Flat membranes can be procured with varying surface characteristics, but printing of complex geometries is nearly impossible.

A much more complex digital light processing system was built using an ATUM 3D kit that included a projector and an Arduino microcontroller, see Figure 16.

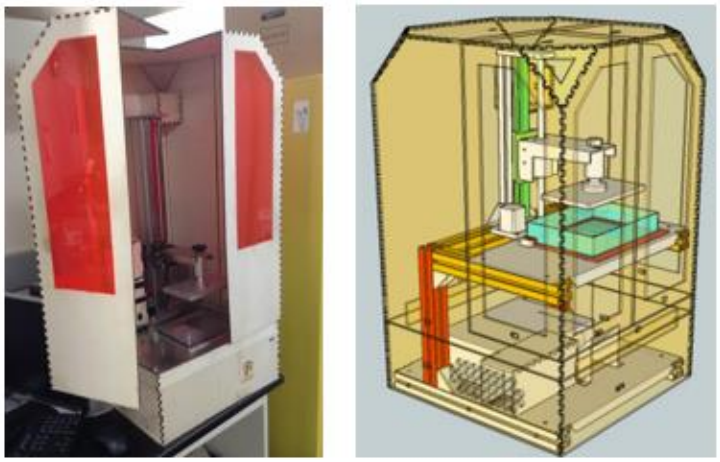

Figure 16: An ATUM 3D printer was used for DLP exposure trials.

The ATUM printer is paired with Creation Workshop Software the facilitate print models created in CAD; any .stl files can be input for printing. The Creation Workshop program is well suited for printing synthesized resins, as virtually all printing parameters can be varied. Users can vary printing times and resolution via layer thickness. Exposure time and intensity can be engineering to produce quality prints for any polymerizable resin, clear or opaque. A secondary monitor can be used to display layer shapes projected during the prints for monitoring the progress of each DLP trial. Resin in the ATUM printer resides in an immobile basin with a high quality clear plastic base to ensure transmittance of focused projector light. The build platform moves on a vertical axis with respect to inputs from the Arduino controller, and the casing blocks all extraneous light from affecting the print. The printer is capable of printing precise, complex objects from a wide variety of polymerizable resins. However,

tailoring the print conditions to each specific resin can be arduous and requires numerous print trials to achieved high printing precision.

The Form 1+ is a commercially available stereolithographic printer suited to pair with desktop software, see Figure 17. Formlabs, a 3D printer manufacturer in Massachusetts, sells the Form 1+ with required software and a small variety of resins.

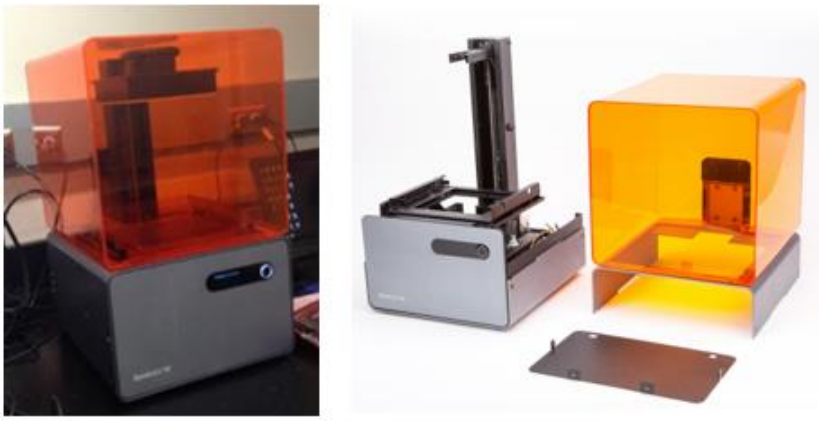

Figure 17: STL trials were performed on a Form 1+ printer by Formlabs.

The printer utilizes a 120 mW, 405nm violet laser with a 155 micron spot size that can be programmed print a layer in a matter of seconds. Unlike the immobile resin basin in the DLP system, the Form 1+ has a hinged resin basin with a motor separate from the build platform motor. The hinge system allows for a peeling process between layers to ensure that printing pieces do not end up on the bottom of the resin basin and fail to print correctly. Printing times can be shortened by limiting print purity and increasing print layer thickness; this STL printer is capable of layer thicknesses from 25 to 200 microns. Seven available resin types include black, castable, clear, flexible grey, tough, and white resins, and each type is inherently suited for different modeling applications.

Synthesized resins can be printed on the From 1+. However, the Formlabs software does not permit adjusted exposure times and intensities which can be problematic for unique resin formulas. The DLP printer can be used to ensure printing is viable on the Form1+ with a specialized resin. Parameters

within the DLP Creation Workshop program are adjusted form the desired resin, and commercial resins are run under the specialized parameters until a successful print is achieved. The synthesized resin can then be used in the Form 1+ with conditions similar to the commercial resin successfully printer on the DLP printer. While this procedure is not full-proof, it is often sufficient for printing simpler geometries.

Printed polymer material strength can be characterized by printing tensile bars for mechanical break tests. Available mechanical testing equipment was located in the Department of Material Science and Engineering at Penn State with the Instron 5866 seen in Figure 18.

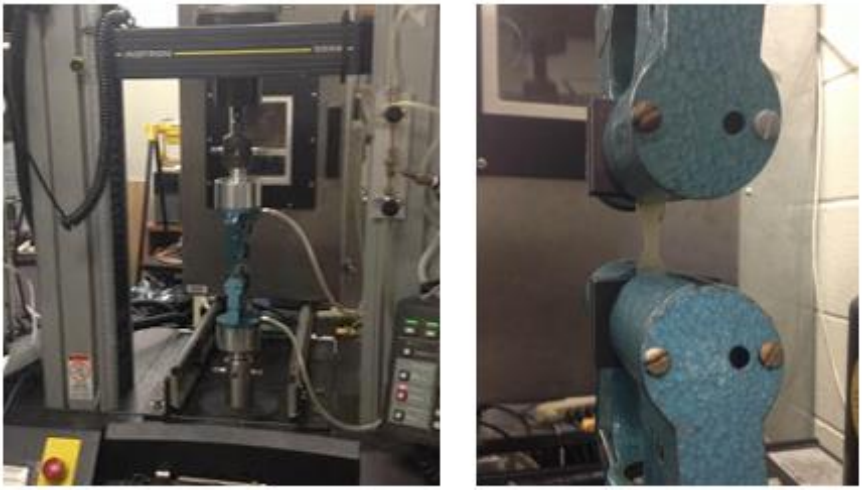

Figure 18: Mechanical break tests were conducted on the Instron 5866.

The Instron 5866 is a mechanical testing product fit for varieties of compression and extension testing, including tensile tests. Pneumatic grips hold tensile bars at constant pressure to limit slippage during material stretching. Load cells capacities vary, and 500N load cells were used for breaking small polymer tensile bars. Bluebook software was paired with the Instron 5866 to facilitate easy data collection and analysis.

Materials

Resin recipes were based on successful printing recipes of other researchers at Penn States 3D printing lab. Synthesis hoods were available for mixing resins, and resins used were primarily a mixture of poly (ethylene glycol) dimethacrylate (PEGDM) and diurethane dimethancrylate seen below.

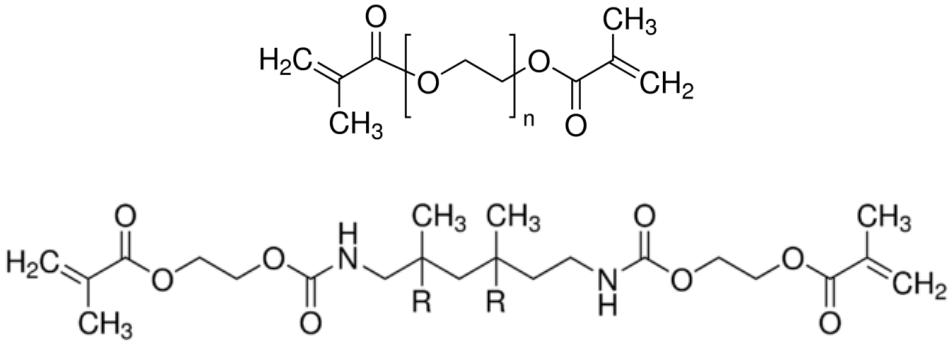

Figure 19: Resins were primarily PEGDM (top) and diurethane dimethancrylate (bottom).

Diurethane dimethacrylate (CAS 72869-86-4) is a viscous polymer while the addition of PEGDM (CAS 25852-47-5) decreases resin viscosity, making it easier to handle and more suitable to print. Small amounts of powdered ketone in the form of [1-hydroxycyclohexyl phenyl] ketone (CAS 947-19-3) and powdered phosphine as Phenylbis (2,4,6,-trimethyl-benzoyl) phosphine oxide (CAS 162881-26-7) were added to the liquid resin. Bromomethylmol blue initiator (CAS 76-59-5) was added to facilitate the photo polymerization reaction under each printing method. All resin types were stored in glass vials impermeable to ultraviolet light.

While composite doping has been used in membrane technology and in separate 3D printing of pieces for optimum mechanical characteristics, composite doping was not implemented at the Penn state 3D print lab. The composites used for doping resins included hydrophobic Nanomer-I.44P, a surface-modified Montmorillonite clay. Produced by Nanocor Inc., the composite powder is 55-65 wt% Montmorillonite clay and 35-45 wt% Dimethyl dialkyl(C14-18) ammonium.

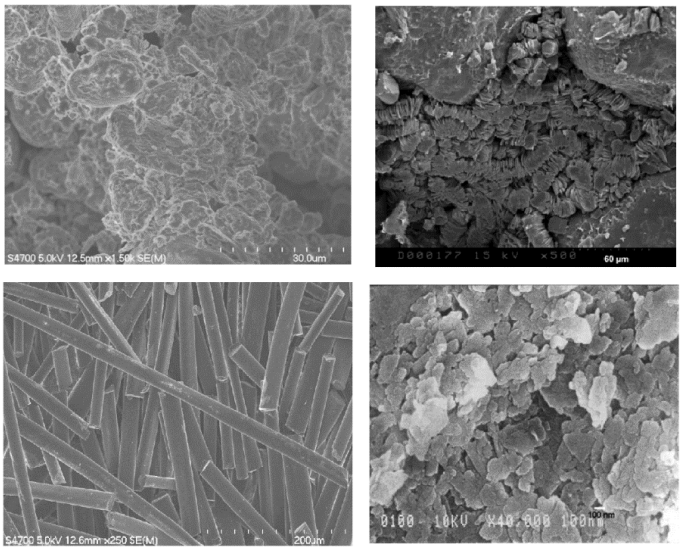

Figure 20: Hydrophobic Nanomer I.44P (left) and hydrophilic Kaolin XP6100 (right) at differing resolutions.[36,37]

A secondary clay sample for doping was hydrophilic, Kaolin XP6100 produced by Imerys. This sample of kaolin clay, rich in $Al_2Si_2O_5$, was a fine powder containing 0.3 wt% sodium polyacrylate. As seen in the SEM images of Figure 20, the nanomer clay (left) has crystalline structure on the scale of several hundred microns, while relatively amorphous on a smaller scale.[36] The kaolin clay (right), on the other hand, forms crystalline platelets roughly one micron across, and is less structured at 100 microns.[37] Clay doping amounts were varied between samples.

Procedure and Results

Resins were synthesized by combining and mixing PEGDM and polyurethane polymers. Ketone, phosphine and photoinitator powders where dissolved into the organic phase easily. The resin formula is provided in Table 2.

Table 2: Resin Formulas

Component	Recipe	Actual wt %
PEGDM	140.0ml	68.5%
polyurethane	60.0 ml	29.7%
ketone	2 g	0.89%
phosphine	2 g	0.89%
blue initiator	120mg	0.05%

Hydrophobic and hydrophilic clays were added to the resins to make samples at 1%, 5%, and 10% by weight of each composite respectively. Mixing the clay powders into the resins was not as straightforward as adding ketone and phosphine powders; due to the low density of the ceramic powders, large wt% samples required rigorous mixing to integrate the additive into the resins. Samples were procured adding clay to roughly 20ml of resin. To increase available resin for printing, a second batch of 20ml samples was created and added to the previous samples. Actual compositions of the combined samples are listed in Table 3; compositions of each batch are listed in Appendix A.

Table 3: Resin Doping: Combined Samples

Identity	Mass 20mL Resin (g)	Theor. Mass Req. (g)	Actual Mass Clay (g)	wt % Composite
10% hydrophilic	44.642	4.9602	4.96	10.00%
5% hydrophilic	44.9273	2.3646	2.3653	5.00%
1% hydrophilic	44.7042	0.4515	0.4527	1.00%
1% hydrophobic	44.3894	0.4484	0.4513	1.01%
5% hydrophobic	44.2858	2.3308	2.3316	5.00%
10% hydrophobic	44.0225	4.8914	4.8891	10.00%

Unused resin was saved for control samples with 0% doping. Composites did not fully dissolve and resulted in clouded resin liquid. After an extended time, the course of several hours, separation occurred to create a clay rich suspension and a relatively clear phase. Resin separation occur more drastically in the samples doped with hydrophobic composites. While a clay suspension could be re-established with stirring, the samples required mixing before each print as separation occurred readily. The resin formula without doping yielded a clear yellow liquid. Hydrophobic doping decrease clarity somewhat and altered the color to a darker semi-clear yellow liquid. Hydrophilic doping decreased resin clarity significantly and lightened the shade of yellow, creating a cloudy, pale-yellow resin.

Membrane samples for each resin doping fraction were printed with the simplified projector-focal lens-mirror setup. Exposure times for each layer were dictated manually at 30 seconds, and printing required constant monitoring. Resins were printed by blotting 1 mL of resin onto a petri dish at a time; after curing several layers, an additional 1 mL of resin was layer above the piece. Each membrane print required 5 mL of resin, and produced membranes are displayed in Figure 21.

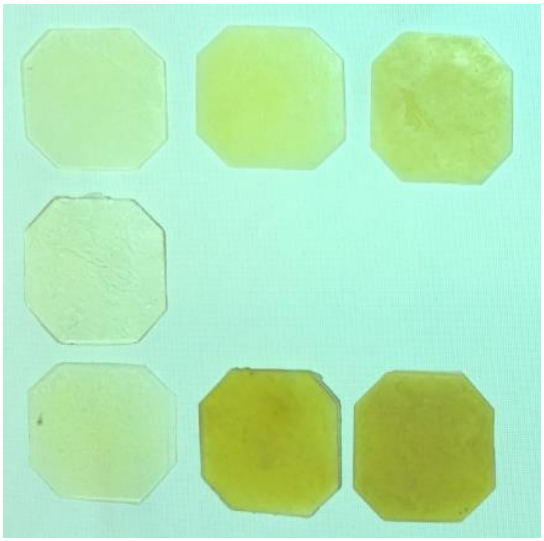

Figure 21: Doping increases left to right: hydrophilic doping (top), control (middle), and hydrophobic (bottom).

Hydrophobic-doped resins were more viscous than their hydrophilic-doped counterparts. Moreover, hydrophobic-doped resins polymerized more readily, albeit more inconsistently, under similar

exposure conditions. Membrane surfaces were smoother for hydrophilic-doped samples, and samples were cured in an ultraviolet oven after exposure. Samples with high doping percentages yielded a greasy surface after the UV curing process, suggesting that high resin doping interferes with the bromomethylmol photoinitiator.

Once the viability of resin printing was established on the simple projector setup, ideal printing conditions were studied on the digital light processing printer. Several iterations of parameter adjustments, including layer thickness and exposure times, were required before perfecting print conditions. Overexposed and under exposed print failures are given below in Figure 22.

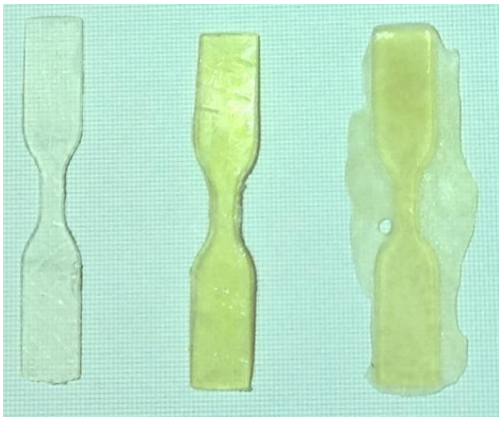

Figure 22: Tensile bars under-exposed (left), at correct exposure (middle), and over exposure (right).

After samples with 1% hydrophobic doping were successfully printed on the DLP systems, motor issues for the build platform prevented the printer from functioning. While hardware issues were investigated, resoldering connections did not fix the issues. Communication problems between the motor, micro-controller, and Creation Workshop programs were likely software issues, and could not be fixed quickly. Tensile bar prints were transferred to the Form 1+ software with the same .stl 3D model file. As the Form 1+ only offers conditions for the commercial Formlabs resin products, DLP printing conditions were matched to commercial resins; exposure rate conditions for the grey Formlabs resin were chosen for printing the synthesized polyurethane-PEGDM resins.

Young's modulus can be used to characterize a material's ability to handle physical stress. The modulus measured stress (force per unit area) over strain (proportional physical deformation). This analysis was applied 3D printed tensile bar samples as seen in Figure 23.

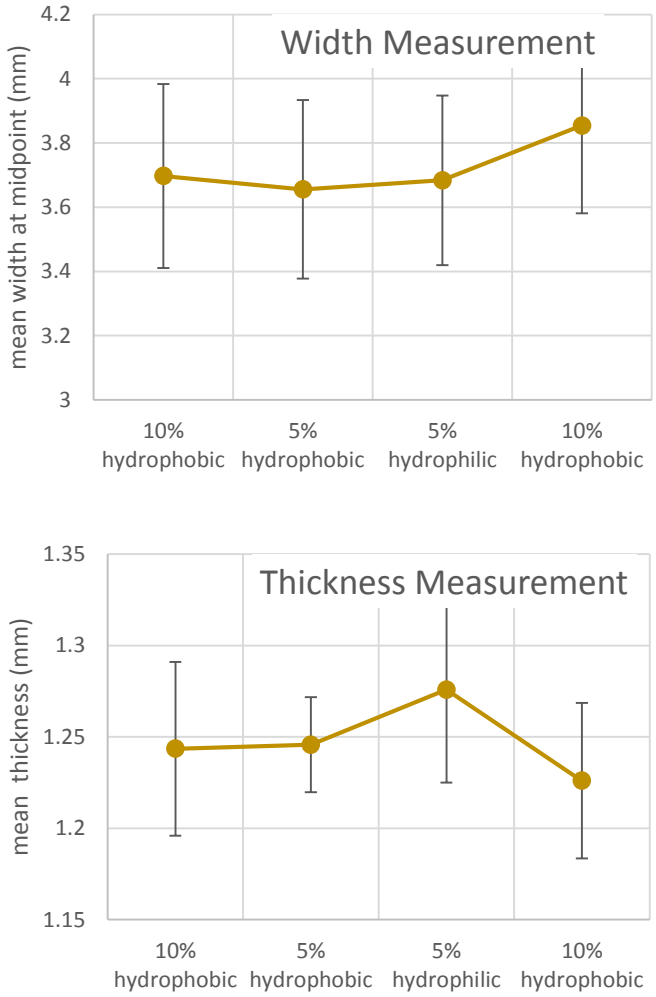

Figure 23: Width and thickness dimensions did not differ with doping.

All tensile bars were printed using the same .stl file. Dimensions of printed bars were measured with calipers and are reported in Appendix A. Considering high weight percent polymers, there is little evidence to suggest that specific composite doping inhibits the precision of the stereolithographic printing method. In Figure 23, mean dimensions for samples are reported with error bars at one standard deviation.

Using the Instron 5866 for mechanical break testing, tensile bar breakpoint data was recorded and process through Bluebook software. An example plot generated during the testing is given in Figure 24 for a control, 0% dope tensile bar.

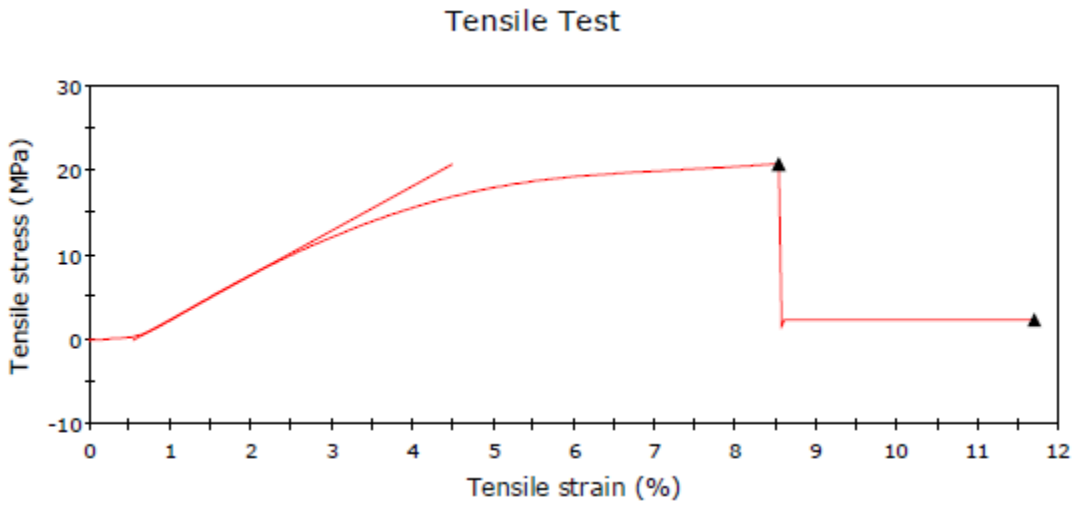

Figure 24: Tensile test curves were used to calculate Young's modulus.

During the mechanical break test, the load cell monitors physical stress as samples were pulled apart. A point was marked at the peak of the curve marks maximum stress, and was compared to a baseline value measured at the end of the curve after tensile break. The linear fit to the tensile test curve displays the method of Young's modulus calculation where the slope gives stress over strain values for each sample. Samples yielded at maximum stress values between 22 and 25 MPa. Commercially available Nafion membranes have demonstrated a tensile strength at 27.7 MPa.[32] While tensile strength values are similar, Nafion exhibits high percent elongation over tensile testing while elongation of PEGDM/polyurethane membranes yielded at only 6 to 11 percent elongation, see Appendix A.

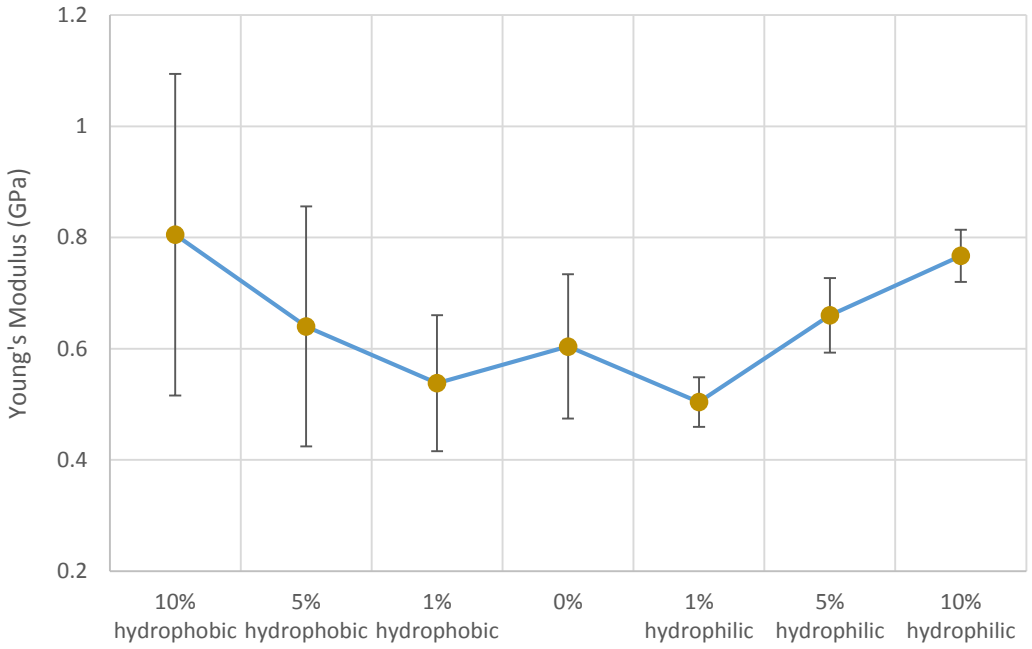

Figure 25: Sample rigidity increased doping. Hydrophobic doping prints were significantly less precise.

Young's modulus was presented for comparing each doped resin in Figure 25, and error bars are marked at one standard deviation. A clear trend exists where the modulus increases with both hydrophilic and hydrophobic doping. In other words, printed resins become more rigid with the addition of clay composites. A similar trend exists with mechanical test data for nanocomposite doping in literature.[31,32] Hydrophilic and hydrophobic additives affect the mechanical properties similarly, but an error bar analysis yields significant information for viable printing techniques.

Considering that all samples were printed under the same conditions, high variance in a set of printed tensile bar displays inconsistent or non-uniform print composition. Given the uniform variance in print dimensions in Figure 23, hydrophobic and hydrophilic clay additives do not affect photopolymerization differently. However, variance in mechanical testing data demonstrates that hydrophobic doping fails to print mechanically uniform pieces where hydrophobic additives permit for a precise set of prints. The inconsistency in hydrophobic prints was likely due to the phase separation noted earlier. When hydrophobic composites do not readily disperse throughout the resin solution,

concentrations of clay deposits vary throughout the liquid resin and throughout the printed object. When considering ideal resins for stereolithographic and digital light processing techniques, the viscous nature of hydrophobic-doped resins requires more laborious sample preparation, mixing, and printer basin cleaning than less viscous counterparts. The opaque nature of hydrophilic-doped resins would be beneficial in producing larger printed objects with complex geometries; incident light would not permeate far into the resin and accurate layer polymerization.would be viable. Electrochemical membranes require high precision with respect to chemical composition, and hydrophilic clay doping maintains this precision while hydrophobic clay doping does not.

Chapter 5 Conclusions

Hydrophobic and hydrophilic clays were added to a poly(ethylene glycol) dimethacrylate and polyurethane resin mixture before photopolymerization. Simplified digital light processing techniques, computer-aided DLP methods, and stereolithography were applied to create three dimensional objects from digital files. Resin properties and mechanical testing emphasized hydrophilic clays as an ideal additive to chosen resins. Hydrophobic clay doping, while possible, yielded prints with inconsistent mechanical properties due to non-ideal dispersal of the clay additive in the resin solution. Composite doping has been utilized to engineer ideal electrochemical properties in proton exchange and polymer electrolyte membranes. Polymer membrane fuel cells and other electrochemical devices could become emergent technologies if material and manufacturing costs are significantly reduced. Further experimentation would involve the creation of ion channels within hydrophilic-doped resins through chemical synthesis. Electrochemical analysis with varying composite concentrations would yield optimum doping conditions for membrane applications.

Appendix A

Resin Doping: Batch 1

identity	mass 20mL resin (g)	theor. mass req. (g)	actual mass clay (g)	wt % composite
10% hydrophilic	22.3857	2.4873	2.4869	10.00%
5% hydrophilic	22.4888	1.1836	1.184	5.00%
1% hydrophilic	22.3266	0.2255	0.2263	1.00%
1% hydrophobic	22.2819	0.2251	0.2270	1.01%
5% hydrophobic	22.1719	1.1669	1.1676	5.00%
10% hydrophobic	21.9128	2.4348	2.4306	9.98%

Resin Doping: Batch 2

identity	mass 20mL resin (g)	theor. mass req. (g)	actual mass clay (g)	wt % composite
10% hydrophilic	22.2563	2.4729	2.4731	10.00%
5% hydrophilic	22.4385	1.181	1.1813	5.00%
1% hydrophilic	22.3776	0.2260	0.2264	1.00%
1% hydrophobic	22.1075	0.2233	0.2243	1.00%
5% hydrophobic	22.1139	1.1639	1.164	5.00%
10% hydrophobic	22.1097	2.4566	2.4585	10.01%

Tensile Bar Dimensions

		wide width (mm)	thin width (mm)	thickness (mm)
hydrophobic	10.1	--	--	--
	10.2	8.376	3.92	1.205
	10.3	8.318	3.661	1.264
	10.4	8.295	3.306	1.301
	10.5	8.538	3.902	1.204
	5.1	8.548	3.694	1.264
	5.2	8.422	3.669	1.226
	5.3	8.187	3.291	1.272
	5.4	8.446	3.967	1.221
	5.5	8.948	4.467	0.682*
	1.1	8.667	3.628	2.023
	1.2	8.447	3.563	1.742
	1.3	8.109	3.637	1.907
	1.4	7.927	3.697	1.802
	1.5	8.465	2.955	1.78*
	0.1	8.177	3.771	1.823
	0.2	8.253	3.551	1.989
no doping	0.3	8.756	3.136	1.971
	0.4	8.909	3.988	1.658
	0.5	8.293	2.557	1.839*
	1.1	8.251	3.244	1.334
	1.2	8.23	3.682	1.279
	1.3	8.413	3.648	1.212
	1.4	8.195	3.573	1.26
	1.5	8.162	3.456	1.323
	5.1	8.662	3.438	1.298
	5.2	8.211	4.052	1.186
	5.3	8.768	3.683	1.288
	5.4	8.137	3.817	1.296
	5.5	8.481	3.429	1.311
	10.1	8.437	3.786	1.186
	10.2	8.601	3.892	1.201
	10.3	8.413	4.299	1.206
	10.4	8.459	3.713	1.291
hydrophilic	10.5	8.464	3.58	1.246
		wide width (mm)	thin width (mm)	thickness (mm)
		MEAN		
hydrophobic	10	8.38175	3.69725	1.2435

	5	8.40075	3.65525	1.24575
	1	8.2875	3.63125	1.8685
no doping	0	8.52375	3.6115	1.86025
	1	8.2502	3.5206	1.2816
	5	8.4518	3.6838	1.2758
hydrophilic	10	8.4748	3.854	1.226
STD DEV				
hydrophobic	10	0.11	0.29	0.05
	5	0.15	0.28	0.03
	1	0.33	0.05	0.12
no doping	0	0.36	0.36	0.15
	1	0.10	0.18	0.05
	5	0.27	0.26	0.05
hydrophilic	10	0.07	0.27	0.04
		*thin samples not included in mean		

Tensile Bar Tests:
Mean Values

	Maximum Load	Extension at Break	Load at Break (Standard)	Elongation	Modulus	Maximum Tensile stress
Units	(N)	(mm)	(N)	(%)	(GPa)	(MPa)
10% hydrophobic	100.92	1.87	9.42	0.06448276	0.805	22.02
5% hydrophobic	97.79	2.64	7.47	0.09428571	0.64	23.18
1% hydrophobic	141.44	3.08	17.58	0.12833333	0.538	23.85
0%	139.49	2.77	18.71	0.11541667	0.604	22.85
1% hydrophilic	100.87	2.66	7.66	0.11083333	0.504	22.35
5% hydrophilic	110.38	2.53	13.07	0.10541667	0.724	24.55
10% hydrophobic	117.67	2.09	10.97	0.08708333	0.767	24.96

Appendix B

The 3D print lab at Penn State is directed by Dr. Mike Hickner and is located in Research Unit A—Modular Lab which is a new, temporary building located off of Hastings Rd.

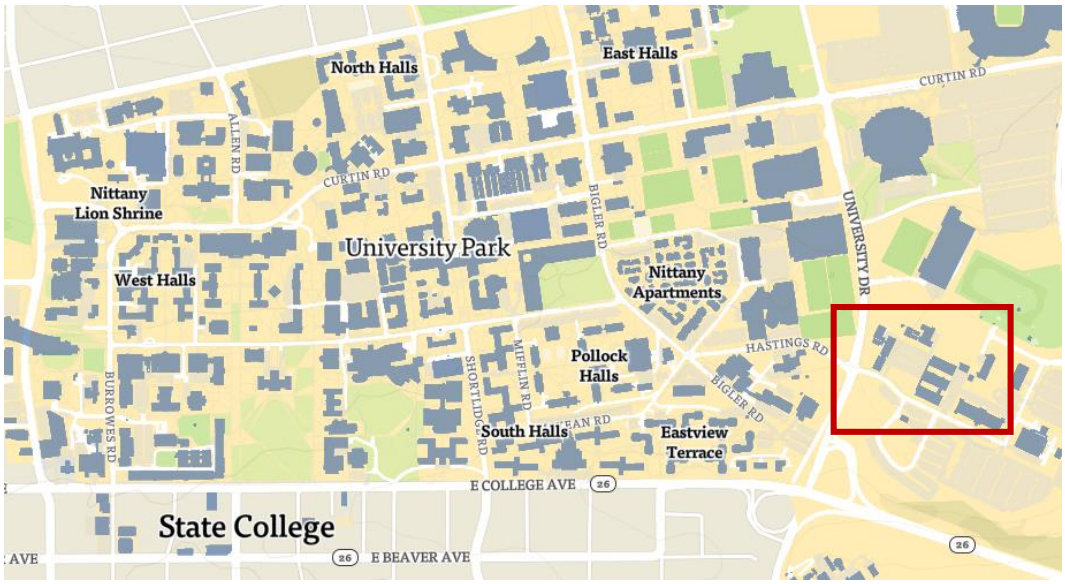

Bibliography

1. D.T. Hallinan, N.P. Balsara, Annu. Rev. Mater. Res. 2013, 43, 503-525.
2. W. Mérida; D. A. Harrington; J. M. Le Canut; G. McLean, J. Power Sources. 2006, 161 (1), 264-274.
3. C. Sequeira; D. Santos, Polymer Electrolytes: Fundamentals and Applications; Woodhead: Cambridge, 2010; Chapter 4, pp 129-168.
4. K. Hooshyari; M. Javanbakht; L. Naji; M. Enhessari. J. Mem. Science. 2014, 454, 74-81.
5. A. Shabanikia; M. Javanbakht; H. S. Amoli; K. Hooshyari; M. Enhessari, Electrochimica Acta. 2015, 154 (1), 370- 378.
6. T.Y. Wu, L. Hao, C.W. Kuo, Y.C. Lin, S.G. Su, P.L. Kuo, I.W. Sun, Int. J. Electrochem. Sci. 2012, 7, 2047-2064.
7. D. Saikia, Y.C. Pan, C.G. Wu, J. Fang, L.D. Tsai, H.M. Kao, J. Mater. Chem. C. 2014, 2, 331-343.
8. F. Croce; G. B. Appetecchi; L. Persi; B. Scrosati, Nature. 1998, 394, 456-458
9. A. Dey, S. Karan, S.K. De, Indian J. Pure Appl. Phys. 2013, 51, 281-288.
10. G.B. Appetecchi, F. Croce, L. Persi, F. Ronci, B. Scrosati, Electrochimica Acta. 2000, 45, 1481-1490.
11. A.M. Stephan, K.S. Nahm, Polym. 2006, 47, 5952-5964.
12. R. Hammami; Z. Ahamed; K. Charradi; Z. Beji; I. B. Assaker; J. B. Naceur; B. Auvity; G. Squadrito; R. Chtourrou, Int. J. Hydrogen Energ. 2013, 38 (26), 11583- 11590.
13. A. M. Stephan; K.S. Nahm, Polymer. 2006, 47 (16), 5952-5964
14. H. Chae, D. Song, Y.G. Lee, T. Son, W. Cho, Y.B. Pyun, T.Y. Kim, J.H. Lee, F. Fabregat-Santiago, J. Bisquert, Y.S. Kang, J. Phys. Chem. C. 2014, 118, 16510–16517.
15. S. Gao, X.L. Yan, J. Zhong, G.B. Xue, B. Wang, Appl. Phys. Lett. 2013, 102, 173903-0-173903-4.
16. R. Kumar, A. Subramania, N.T.K. Sundaram, G.V. Kumar, I. Baskaran, J. Membr. Sci. 2007, 300, 104-110.
17. M. Han; J. H. Xu; S.H. Chan; S. P. Jiang, Electrochimica Acta. 2008, 53 (16), 5361-5367.
18. M.M. Emami; F. Barazandeh; F.Yaghmaie, Sensors Actuators A: Phys. 2014, 218, 116-124.
19. F.P.W. Melchels; J. Feijen, D.W. Grijpma, Biomat. 2010, 31 (24), 6121-6130.
20. J. Lee; W.S. Tan; J. An; C.K. Chua; C.Y. Tang; A.G. Fane; T.H. Chong, J. Mem. Sci. 2016, 499, 480-490.

21. R. Liska ; M. Schuster; R. Inführ; C. Turecek; C. Fritscher; B. Seidl; V. Schmidt; L. Kuna; A. Haase; F. Varga; H. Lichtenegger; J. Stampf. J. Coat. Tech. Res. 2007, 4 (4), 505-510.

22. A. Boschetto; L. Bottini; F. Veniali. Rob. Comp.-Int. Manuf. 2016, 41, 92-101.

23. S. Kumar. Comp. Mat. Proc. 2014, 10, 93-134.

24. R. Ganeriwala; T. Zohdi. Procedia CIRP. 2014, 14, 299-304.

25. G. Guan; M. Hirsch; Z.H. Lu; D.T.D. Childs; S.J. Matcher; R. Goodridge; K.M. Groom; A.T. Clare. Mat. & Des. 2015, 88, 837-846.

26. P. Heinl; L. Muller; C. Korner; R.F. Singer; F.A. Muller. Acta Biomaterialia. 2008, 4 (5), 1536-1544.

27. M.F. Zah; S. Lutzmann; Prod. Proc. 2010, 4 (1). 15-23.

28. G. Baudana; S. Biamino; B. Klodem; A. Kirchner; T. Weibgarber; B. Kieback; M. Pavese; D. Ugues; P. Fino; C. Badini. Intermetallics. 2016, 73, 43-49.

29. B. Mueller; D. Kochan. Comp. in Ind. 1999, 39 (1), 47-53.

30. H. Philamore; J. Rossiter; P. Walters; J. Winfield; I. Ieropulos. J. Power Sources. 2015, 289, 91-99.

31. T. Agag; T. Koga; T. Takeichi. Polymer. 2001, 42 (8), 339-3408.

32. S.B. Lee; Y.J. Kim; U. Ko; C.M. Min; M.K. Ahn; S.J. Chung; I.S. Moon; J.S. Lee. J. Mem. Sci. 2015, 456, 49-56.

33. Y. Yin; S. Hayashi; O. Yamada; H. Kita; K.I. Okamoto. Macro. Rapid Comm. 2005, 26 (9), 696-700.

34. S. K. Kim; C. A. Guymon. Polymer. 2012, 53, 1640-1650.

35. H. Tan; D. Yang; J. Han; M. Xiao; J. Nie. App. Clay Science. 2008, 42, 25-31.

36. H. Yao; Z. You; L. Li; S.W. Goh; C.H. Lee; Y.K. Yap; X. Shi. Constr. Build. Mat. 2013, 38, 327-337.

37. M.J. Wilson; L. Wilson; I. Patey. Clay Minerals. 2014, 49, 147-164.

ACADEMIC VITA

Academic Vita of Christopher Malencia
cxm5265@psu.edu

Education

Major(s) and Minor(s):	B.S in Chemical Engineering, Minor in Electrochemical Engineering
Honors:	Chemical Engineering
Thesis Title:	INCORPORATING NANOSCALE COMPOSITES INTO STEREOLITHOGRAPHIC PRINTING TECHNIQUES FOR THE OPTIMIZATION OF MEMBRANE ELECTROCHEMICAL PROPERTIES
Thesis Supervisor:	Michael Hickner
Work Experience: Date	September 2013 – October 2014 Undergraduate Researcher Investigations into organic char adsorption for catalysis Earth and Mineral Sciences Energy Institute, Penn State P.I. Dr. Angela Lueking

Awards:

John R. and Jeanette Dachille McWhirter Student Excellence Fund in Chem. Engineering

Richard H. and Kay W. Klingler Scholarship in Chemical Engineering

Eagle Scout Award

Publications:

A.D. Lueking; C-Y, Wang; S. Sircar; C. Malencia; H. Wang; J. Li, A generalized adsorption-phase transition model to describe adsorption rates in flexible metal organic framework RPM3-Zn, *Dalton Tran*., 2015, 00, 1-16.